Vector Electrometry in a Wide-Gap-Semiconductor Device Using a Spin-Ensemble Quantum Sensor

Bang Yang,[1] Takuya Murooka,[1] Kosuke Mizuno,[1] Kwangsoo Kim,[1] Hiromitsu Kato,[2]
Toshiharu Makino,[2] Masahiko Ogura,[2] Satoshi Yamasaki,[2] Marek E. Schmidt,[3] Hiroshi Mizuta,[3]
Amir Yacoby,[4,5,6] Mutsuko Hatano,[1] and Takayuki Iwasaki[1,*]

[1]*Department of Electrical and Electronic Engineering, School of Engineering, Tokyo Institute of Technology, Meguro, Tokyo 152-8552, Japan*

[2]*Advanced Power Electronics Research Center, National Institute of Advanced Industrial Science and Technology, Tsukuba, Ibaraki 305-8568, Japan*

[3]*School of Materials Science, Japan Advanced Institute of Science and Technology, 1-1 Asahidai, Nomi, Ishikawa 923-1292, Japan*

[4]*Department of Physics, Harvard University, 17 Oxford Street, Cambridge, Massachusetts 02138, USA*

[5]*John A. Paulson School of Engineering and Applied Sciences, Harvard University, Cambridge, Massachusetts 02138, USA*

[6]*Tokyo Tech World Research Hub Initiative (WRHI), School of Engineering, Tokyo Institute of Technology, Meguro, Tokyo 152-8552, Japan*

Nitrogen-vacancy (N-V) centers in diamond work as a quantum electrometer. Using an ensemble state of N-V centers, we propose vector electrometry and demonstrate measurements in a diamond electronic device. A transverse electric field applied to the N-V axis under a high voltage is measured, while applying a transverse magnetic field. The response of the energy-level shift against the electric field is significantly enhanced compared with that against an axial magnetic field. Repeating the measurement of the transverse electric field for multiple N-V axes, we obtain the components of the electric field generated in the device.

I. INTRODUCTION

The electric field is a driving force of systems in a variety of fields, such as electronic devices, electrochemical reactions, and cell membranes. Detecting the electric field inside such systems is a challenging task. High-resolution electrometry can be performed using a scanning probe microscope [1,2] with the capability of making vector measurements [3]. However, these methods only give information at the vicinity of the surface. Recently, electron spins in solid-state materials, such as nitrogen-vacancy (N-V) centers in diamond [4–18] and divacancies in SiC [19,20], have emerged as electrometers. The N-V center is a complex defect composed of a pair of a nitrogen atom and a neighboring vacancy in diamond [21]; it also works as a quantum sensor for magnetic fields [22–24], temperature [25–29], and pressure [30]. N-V-based electrometry was first reported by Van Oort and Glasbeek [4], in which they determined the electric dipole moments of the N-V center. Dolde *et al.* [5] reported the measurement of axial and transverse electric fields using a single N-V center. However, the axial electric susceptibility factor is much lower

than that of the transverse parameter. Thus, usually, the electric field transverse to one N-V alignment is measured for electrometry [10,11], hindering the gathering of vector information on the electric field, which will provide a deeper insight into the operation of the systems.

The ac vector electrometry is demonstrated at 20 K using divacancies in SiC [20]. Room-temperature dc vector electrometry is proposed using an ensemble state of N-V centers with multiple N-V axes [10]. In the proposed method, a transverse magnetic field is applied to one of four N-V axes, while the other three N-V axes suffer from a large axial magnetic field, which significantly lowers the shift of the energy level against the electric field. In this study, we propose a method to overcome this issue. Multiple N-V axes are selected as target N-V centers. A transverse magnetic field is applied to one of the target N-V alignments and, then, an electric field is also generated in the system, giving rise to an electric field transverse to the target N-V. By changing the target N-V axis and by repeating the process, the components of the electric field can be estimated using the information from multiple N-V axes. Here, we demonstrate dc vector electrometry in a diamond electronic device using ensemble N-V centers. Diamond-powered devices are promising candidates for

*iwasaki.t.aj@m.titech.ac.jp

next-generation low-loss power electronics because of their wide band gap, high carrier mobilities, and high thermal conductance [31]. The wide band gap of diamond makes it possible to sustain a high electric field. However, most of the reported diamond devices do not attain an ideal electric field [32], requiring direct detection of the electric field. Furthermore, diamond devices work as a platform for electrical control and sensing for quantum technologies [33–40], in which the internal electric field plays an important role in the operation of the devices. N-V electrometry can provide direct information about the electric field inside the devices. Different from our previous work using single N-V centers [9], here, the spatial distribution of the electric field is observed with an ensemble of N-V centers.

II. PRINCIPLE OF VECTOR ELECTROMETRY

The important characteristics of the N-V center for vector electrometry are the four possible crystallographic

alignments of the N-V axis in the crystal (double alignments exist when considering the N-V and V-N directions). Since a N-V axis takes one alignment of [111], [$\bar{1}1\bar{1}$], [$1\bar{1}\bar{1}$], or [$\bar{1}\bar{1}1$], as shown in Fig. 1(a), ensemble N-V centers include all alignments. The V-N direction of N-V A is consistent with the z axis and that of N-V B is on the x-z plane in the lab frame shown in Fig. 1(d). Notably, for analysis of the electric field, we use a different coordinate for each N-V alignment from that in the lab frame. For each N-V coordinate, the z axis is defined as the direction from the N atom to vacancy, the x axis is perpendicular to the z axis, and the x-z plane includes one of the carbon atoms neighboring the vacancy [7]. In this study, the (x, z) coordinate for N-V A is the ($\bar{1}\bar{1}\bar{1}$, $\bar{1}\bar{1}2$) direction. Similarly, the (x, z) coordinate for N-V B corresponds to the (112, $11\bar{1}$) direction.

We can perform vector electrometry by using multiple N-V axes, similar to vector magnetometry [41,42]. To recognize the relationship between the N-V axes and ODMR
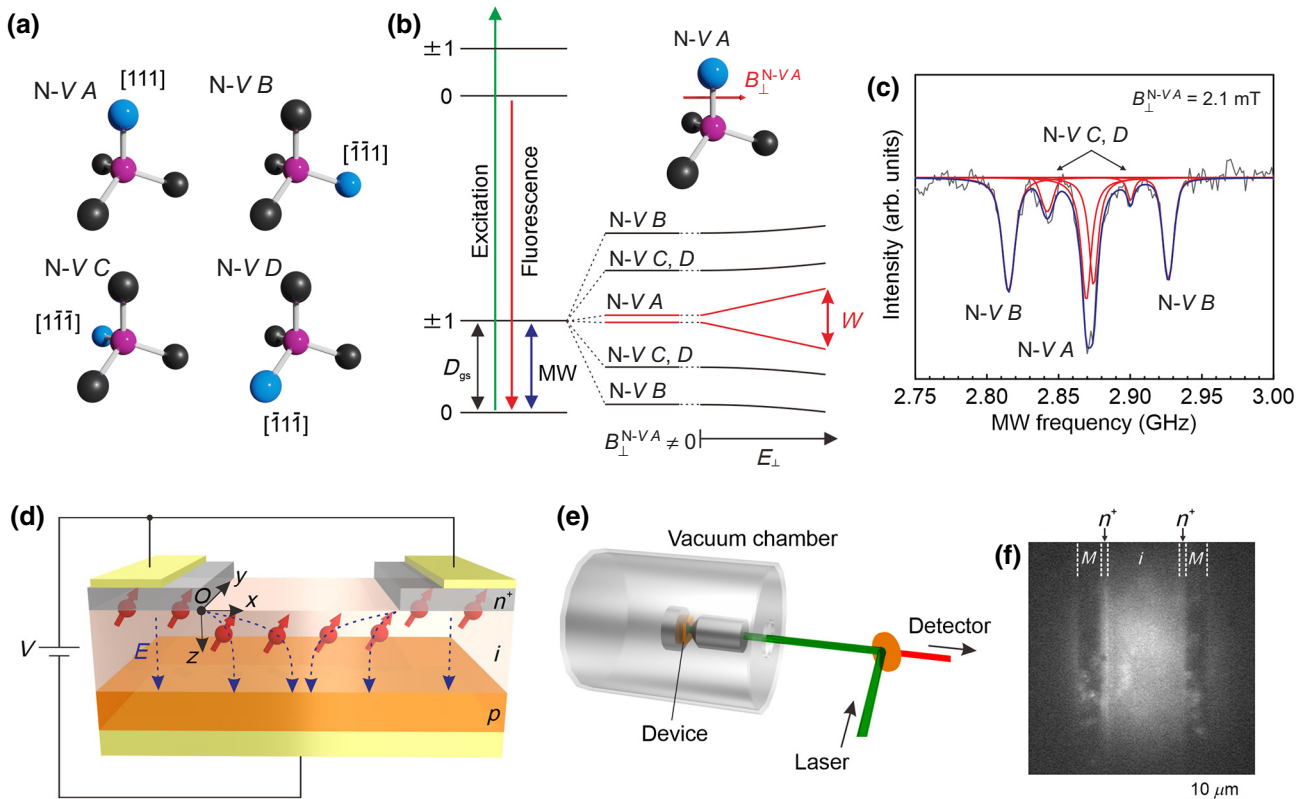

FIG. 1. Vector electrometry using ensemble N-V centers. (a) Four possible N-V alignments. Blue, pink, and black spheres represent N, V, and C atoms, respectively. (b) Energy level of the N-V center. Energy splitting in the ground state is shown for the application of transverse magnetic and electric fields to N-V A. (c) Optically detected magnetic resonance (ODMR) spectrum under a transverse magnetic field of 2.1 mT to N-V A. Gray curve represents experimental data. Red and blue curves are the fits and envelope of the fitting curves, respectively. (d) Vertical diamond p-i-n diode on a (111) diamond substrate, incorporating the N-V centers. "O" denotes the origin of the x-y-z axes in the lab frame. The x and z axes are along [$\bar{1}\bar{1}2$] and [$\bar{1}\bar{1}\bar{1}$] directions, respectively. Dashed lines indicate expected electric fields generated in the i layer of the device. Notably, N-V centers shown as red objects are fabricated uniformly along the y direction, but they are omitted in this figure for the sake of clarity. (e) Measurement setup. Laser goes into the chamber along the z axis in the lab frame, as shown in (d). (f) CCD image of the fluorescence intensity in a device. M denotes cathode metal electrodes on top of the n^+ regions.

signals, an arbitrary directed magnetic field is applied for vector magnetometry. However, for electrometry, the axial magnetic field significantly lowers the shift of the ODMR dips resulting from an electric field (Appendix A). This issue can be overcome using an approach of applying a transverse magnetic field to a N-V axis [Fig. 1(b)] [10,11]. For instance, upon application of a transverse magnetic field to N-V A, the corresponding ODMR signals remain close to the zero-field splitting (D_{GS}), while other N-V axes (N-V B-D) are largely split by axial magnetic fields. Thus, we can recognize the signals from N-V A. Figure 1(c) shows an ODMR spectrum, while applying a transverse magnetic field along the x axis in the lab frame, i.e., [$\bar{1}\bar{1}2$] direction, to N-V A. The direction of the magnetic field is controlled by using three-axis electromagnets (Appendix B). The innermost two dips at about 2.87 GHz in the spectrum correspond to N-V A, while other signals come from N-V B-D.

Then, the N-V A resonance splits further with the application of a transverse electric field [Fig. 1(b)]. The splitting width of ODMR, W, of N-V A is described in Eq. (1) [5,7] (see also Appendix A), taking B_y, $B_z \sim 0$ in the N-V A coordinates:

$$\frac{1}{2}W = \left[k_\perp^2 \Pi_\perp^2 - \frac{\gamma^2 B_\perp^2}{2 D_{\mathrm{GS}}} k_\perp \Pi_\perp \cos \phi_\Pi + \frac{\gamma^4 B_\perp^4}{4 D_{\mathrm{GS}}^2} \right]^{\frac{1}{2}},$$
(1)

where γ denotes the gyromagnetic ratio, provided as 28 GHz/T; $B_\perp$ represents the transverse magnetic field to the N-V axis, defined as $B_\perp = \sqrt{B_x^2 + B_y^2}$; and $k_\perp$ denotes the transverse electric susceptibility parameter, provided as 17 Hz/V/cm [4]. $\Pi_\perp$ is the effective electric field perpendicular to the N-V axis, defined as $\mathbf{\Pi}_\perp = \mathbf{E}_\perp + \boldsymbol{\sigma}_\perp$, where $E_\perp$ and $\sigma_\perp$ are the transverse electric and strain fields, respectively. The magnitude of $\mathbf{\Pi}_\perp$ is given as $\Pi_\perp = \sqrt{\Pi_x^2 + \Pi_y^2}$ and $\tan \phi_\Pi = \Pi_y / \Pi_x$. It is found that the two N-V orientations, i.e., N-V and V-N, take different splitting widths [7,10,43]. We expect that ion implantation and annealing reasonably lead to equal fabrication of the two N-V orientations in the ensemble state. Based on Eq. (1), the estimated difference in the resonance frequency is below 2.5 MHz under the measurement conditions in this study. Furthermore, inhomogeneous broadening of the ODMR signals will occur because the expected electric field strength continuously varies in the range of 180 kV/cm and higher at the high-field region (Fig. 5) and it also varies in the z direction, hindering the observation of the small shift owing to the N-V orientations. Thus, here, we analyze the experimentally obtained ODMR splitting as the average of the two orientations. According to Eq. (1), the splitting increases almost linearly with the electric field, as shown by the solid lines in Fig. 4. At an electric field of about 1.1 MV/cm, the split increase becomes

larger than 30 MHz, compared with about 3 MHz for the case with an axial magnetic field of 4.1 mT used for N-V B (Appendix A). Therefore, the response to the electric field can be increased by a factor of 10 in this field range.

The abovementioned process is related to one N-V axis. Vector electrometry can be achieved by repeating this process for multiple N-V axes, i.e., applying a transverse magnetic field to a target N-V axis and then applying the electric field in the system. Finally, the electric field generated in the device can be estimated from the following system of equations:

$$E_\perp^{\mathrm{N}\text{-}Vi} = |\mathbf{E} - (\mathbf{E} \cdot \mathbf{u}_{\mathrm{N}\text{-}Vi})\mathbf{u}_{\mathrm{N}\text{-}Vi}| \quad (i = A, B, C, D), \quad (2)$$

where $E_\perp^{\mathrm{N}\text{-}Vi}$ is the transverse electric field to each N-V alignment, $\mathbf{E} = (E_x, E_y, E_z)$ in the lab frame, and $\mathbf{u}_{\mathrm{N}\text{-}Vi}$ is the unit vector in each N-V direction (Appendix C). In this study, we use two N-V axes of N-V A and N-V B to obtain E_x and E_z.

III. DEVICE STRUCTURE AND MEASUREMENT SETUP

We perform vector electrometry in a diamond device using ensemble N-V centers. Figure 1(d) shows a vertical diamond p-i-n diode on a boron-doped ([B] $= 1 \times 10^{17}$ cm^{-3}) (111) diamond single-crystal substrate. In terms of electrical properties, the device shows a high rectification ratio of about 10^6 at ± 10 V (Appendix D). The detailed fabrication process of the device is described elsewhere [9,44]. The device has patterned heavily phosphorus-doped ([P] $= 1 \times 10^{19}$ cm^{-3}) 350-nm-thick n^+ regions on top of a 5-μm-thick intrinsic layer. We take one edge of the n^+ region as the origin "O" for the x-y-z axes in the lab frame, as shown in Fig. 1(d). The x and z axes in the lab frame are along the [$\bar{1}\bar{1}2$] and [$\bar{1}\bar{1}\bar{1}$] directions, respectively. The spacing between the n^+ regions is 10 μm. Nitrogen-ion implantation is performed over the device with a dose of 1×10^{12} cm^{-2} and an acceleration energy of 350 keV at an elevated temperature of 600 °C, giving rise to a projected depth of about 350 nm. Then, the device is annealed at 750 °C for 30 min to promote the diffusion of vacancies and form the N-V centers. Thus, ensemble N-V centers are formed in the i layer 350 nm from the surface and at the interface between the n^+ regions and i layer. The diamond substrate with the devices is placed in a vacuum chamber with a quartz window for optical access [Fig. 1(e)]. The vacuum environment ($\sim 6 \times 10^{-3}$ Pa) is used to avoid discharge in air at a high voltage of 400 V. The N-V centers are excited using a 532 nm green laser through an objective lens (numeric aperture: 0.95) placed on three-axis piezo scanners in the chamber, and their fluorescence is measured with a charge-coupled device (CCD) [Fig. 1(f)]. Microwave (MW) radiation is applied though a Cu

wire for electron-spin resonance. All experiments in this study are performed at room temperature.

The arrows with dashed lines in the *i* layer shown in Fig. 1(d) denote the expected electric field generated in the device upon the application of a high reverse voltage. Below the n^+ regions, the electric field in the *z* direction is dominant in the *p-i-n* diode. On the other hand, the electric field concentrates at the edge of the patterned n^+ regions, and thus, has components in both the *x* and *z* directions. At a high voltage of 400 V, the directions of E_x and E_z are positive at the measurement position (Appendix E). The length of the n^+ regions along the *y* axis is 50 μm, and the electric field measurements are performed close to the *y* center. Thus, we assume no electric field in the *y* direction along the electrode, and the binning of the pixels in the *y* direction is performed for the electric field analysis.

IV. VECTOR ELECTROMETRY IN A DIAMOND ELECTRONIC DEVICE

Before the application of the electric field, the magnitude of the transverse magnetic field applied to a target N-*V* alignment (here, N-*V* A) is estimated. The six resonant signals are observed in the ODMR spectrum shown in Fig. 1(c). Since the magnetic field is applied along the *x* axis in the lab frame, i.e., the $[\bar{1}\bar{1}2]$ direction, the outermost signals at 2.82 and 2.93 GHz correspond to N-*V* B. Due to the symmetry of N-*V* C and N-*V* D, their energy levels are degenerate, appearing at the same frequencies of 2.84 and 2.90 GHz. The magnitude of the transverse magnetic field applied to N-*V* A is estimated to be 2.1 mT from the splitting width of the N-*V* B signals.

Then, we apply a reverse voltage to the device, while applying the transverse magnetic field to target N-*V* A. Figure 2 shows the ODMR spectra of N-*V* A at different voltages of 0, 200, and 400 V at the edge of the n^+ region. The split width increases with increasing voltage, implying that the electric field is detected based on this technique. The signal at 400 V is fitted with four dips, as discussed below. Notably, the microwave wire position is adjusted at each measurement, leading to the variation of microwave power applied to the N-*V* centers, and thus, influencing the ODMR contrast.

Next, vector electrometry is performed at a reverse voltage of 400 V using multiple N-*V* axes. Figure 3(c) shows the ODMR spectra depending on the *x* position in the device from the first target of N-*V* A [Fig. 3(a)]. The spatial resolution here is expected to be of micrometer scale (Appendix F). The position at $x = 5$ μm corresponds to the midpoint of the *i* layer between the n^+-diamond regions, where the lowest electric field is expected along the *x* axis. Approaching the edge of the n^+ region [$x = 0$ μm or *O* point in Fig. 1(d)] should increase the electric field due to the field concentration. In the case of taking N-*V* A as a target [Fig. 3(c)], a pair with a large splitting appears in
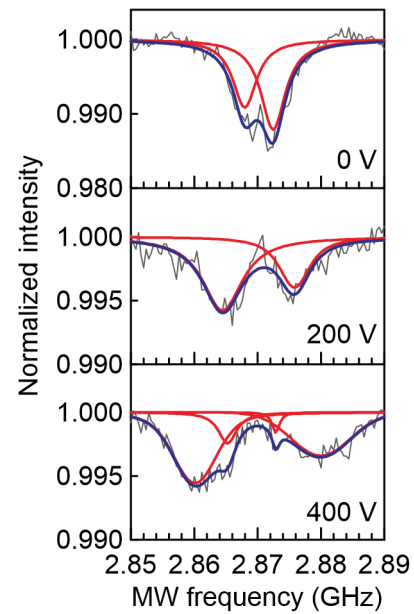

FIG. 2.   ODMR spectra of N-*V* A under reverse voltages and a transverse magnetic field. The measurements were performed at the n^+-edge region. The gray curve represents the experimental data. The red and blue curves are the fits and envelopes of the fitting curves, respectively.

the ODMR spectrum at $x = 2$ μm, and its splitting becomes even larger at $x = 0$ μm by sensing E_x, labeled as f_1^- and f_1^+. Another pair with smaller splitting (f_2^- and f_2^+) would come from N-*V* A at a small electric field position either in the n^+ region, including the n^+-*i* interface, or in the *i* layer. For instance, at a position 20 nm inside the n^+ region for $x < 0$, both E_x and E_z dramatically decrease due to the high P concentration. Notably, the narrow line width of the inner signal is probably because the N-*V* centers at a low electric field position do not suffer from inhomogeneous broadening, but further investigation is required to understand this in more detail.

Then, in the same way, we apply a transverse magnetic field of 4.1 mT to the next target axis, N-*V* B [Fig. 3(b)]. The E_z value is expected to be higher than that of E_x in the *p-i-n* diode. Hence, a higher magnetic field is applied for the case of N-*V* B to avoid overlap of the N-*V* B signals with those from other N-*V* axes upon application of the electric field. Upon the application of 400 V, the ODMR spectra at $x = 5$ and 2 μm show similar signals [Fig. 3(d)]. At $x = 0$ μm, however, the splitting width rapidly increases and multiple signals are observed. The signals considered as pairs are fitted here. Compared with E_x, the large E_z component is generated in the vertical device structure. Thus, the outermost signals (f_1^- and f_1^+) are thought to originate from N-*V* B at the n^+-*i* interface. The pair with the second largest splitting (f_2^- and f_2^+) would correspond to N-*V* B in the *i* layer close to the n^+ edge. The innermost signals (f_3^- and f_3^+) would come from N-*V* B
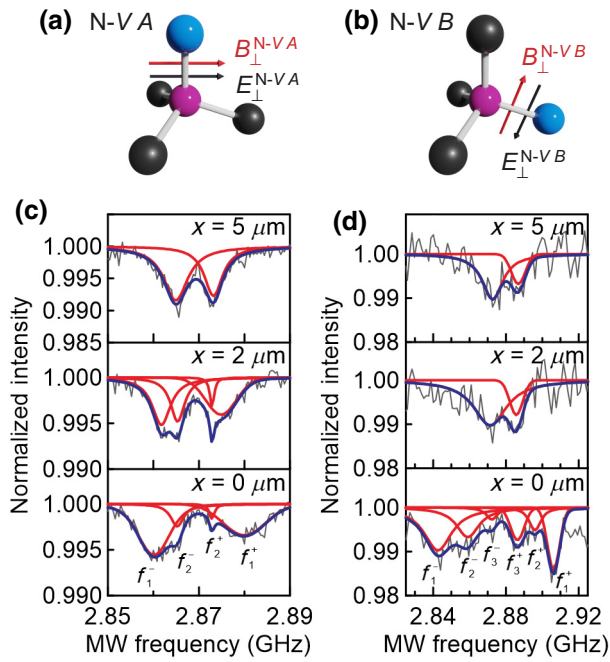
FIG. 3. ODMR spectra under transverse magnetic and electric fields. A reverse voltage of 400 V was applied. Schematics of (a) N-V A and (b) N-V B. ODMR spectra of (c) N-V A and (d) N-V B at different x positions. A reverse voltage of 400 V was applied to the device to generate the electric field. A higher microwave power was used for the N-V B measurements. The gray curve represents the experimental data. The red and blue curves are the fits and envelopes of the fitting curves, respectively.
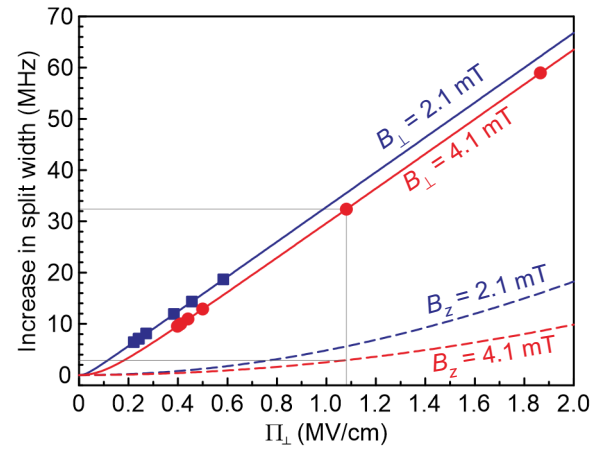

FIG. 4. Increase in the split width of the ODMR dips as a function of the effective electric field. Increase in the split width is defined as the increase from the value at zero effective electric field. Lines indicate calculated values upon application of transverse (solid lines) or axial (dashed lines) magnetic fields to a target N-V. Gray lines represent a comparison of the increase in split width, depending on the direction of the magnetic field.

at a small electric field position inside the n^+ region. When we compare the splitting width in the i layer at $x = 0$ μm, that of the N-V A target is approximately 20 MHz, while that of N-V B is almost doubled, at 37 MHz. We note that the ODMR spectra at $x = 5$ and 2 μm for N-V B show larger noise compared with that of other spectra. This is because the measurement time for N-V B ($\sim$200 s) is shorter than that for N-V A ($\sim$2300 s) to suppress the sample drift, and the center of the excitation laser is close to the n^+ edge for N-V B, while it is in the middle of the i layer for N-V A.

Figure 4 shows the relationship between the increase in the ODMR splitting and the effective electric field ($\Pi_\perp$). The solid lines represent the theoretical values based on Eq. (1). Upon application of the transverse electric field, we see nonlinear behavior at approximately zero, but it becomes a linear dependence over 0.1 MV/cm. The plots depict the experimentally obtained ODMR splitting widths, including the estimates at the n^+-i interface. We can estimate the effective electric field from the experimental splitting width and theoretical curves. The effective electric field is estimated to range from 0.2 to 1.9 MV/cm at a voltage of 400 V.

The effective electric field ($\Pi_\perp$) is composed of the electric field ($E_\perp$) and strain field ($\sigma_\perp$). Due to the unknown

direction of the strain field, we consider the strain field to be an error for the estimation of the electric field. The magnitude of the strain field is obtained from the splitting of the target N-V center at the zero-voltage condition [Fig. 1(c)]. A N-V A splitting width of 4.6 MHz corresponds to about 0.13 MV/cm. Notably, since we do not know the azimuthal angle of strain (ϕ_σ) in Eq. (1), we take the maximum strain value at $\phi_\sigma = 0°$ as an error. The splitting of N-V B is 7.9 MHz, giving rise to a strain field of about 0.2 MV/cm.

Finally, solving Eq. (2) for N-V A and N-V B, we obtain E_x and E_z generated in the device. These values are plotted as a function of the x position in Figs. 5(b) and 5(c). As seen in Fig. 5(b), data at $x > 0$ and $x < 0$ correspond to the electric field in the i layer and n^+-i interface, respectively. The values in the i layer and n^+-i interface are plotted at $x = 0$. Each plot includes information on the continuously varied electric fields on the micrometer scale. The maximum electric fields in the i layer at $x = 0$ μm are $E_x = (0.58 \pm 0.13)$ MV/cm and $E_z = (1.35 \pm 0.26)$ MV/cm. We compare the obtained values with those calculated by the device simulation, as shown by lines in Figs. 5(b) and 5(c). For device simulation, two structural models are considered. Model 1 represents a normal vertical p-i-n diode, while, in model 2, a N donor distribution is added to the device, corresponding to the distribution of N-ion implantation (Appendix E). The substituted N atoms without a neighboring vacancy function as donors in diamond, with a donor level of about 1.6 eV from the minimum of the conduction band. The N atoms introduced by ion implantation are thought to take the donor state, to some extent. In model 2, all implanted N atoms are assumed to be in the donor state, which forms
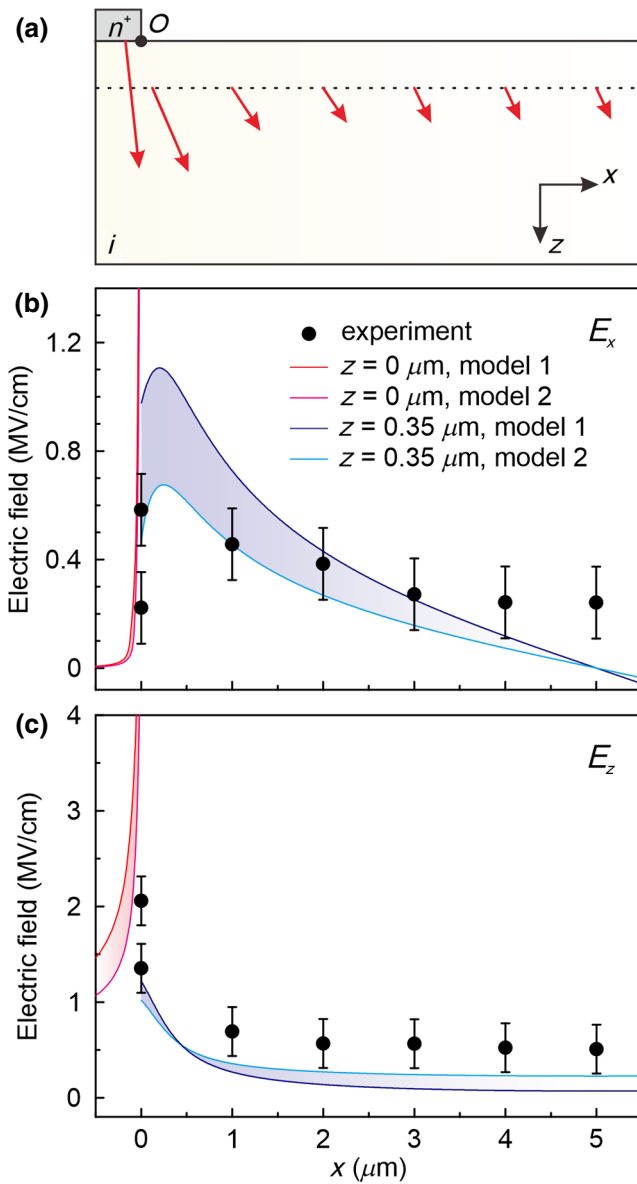
FIG. 5. Comparison with simulation. (a) Schematic of the device with experimentally estimated electric field vectors. Length of red arrows denotes the magnitude of the electric field. Dashed line indicates $z = 0.35$ μm. Two vectors at $x = 0$ μm are shifted for the sake of clarity: (b) E_x and (c) E_z. Dots and lines denote experimental and simulation results, respectively. In model 2, the implanted N atoms are treated as donors in diamond.

one boundary for the simulation. Here, the effects of surface defects [10] and other nitrogen-related defects are not considered. The simulated curves represent the values at the projected depth of the N atoms in the i layer ($z = 0.35$ μm for $x > 0$) and at the n^+-i interface ($z = 0$ μm for $x < 0$). Both the experimental and simulation results increase upon approaching the n^+ edge at $x = 0$ μm.

The experimental estimation of E_x near the n^+ edge is within the simulation results and close to the model that includes the effect of the N donors. The lower limits of E_z, corresponding to the case for the same direction of electric and strain fields, are in good agreement with the simulation. The electric fields that are expected to correspond to the n^+-i interface plotted at $x = 0$ μm are close to the simulation at $z = 0$ μm, when averaged within a few hundred nanometers in the x direction. It is worth noting that the electric fields take much higher values at exactly the n^+ edge in the simulation, but the number of N-V centers at such a region is substantially small. Thus, the value that we obtain experimentally here should be the average of the measurement regions. Figure 5(a) depicts the electric field vectors obtained from the experimental results, clearly showing that the x component is largely generated in the i layer at $x > 0$ μm, while the z component is dominant at the n^+-i interface. Here, we estimate the components of the electric fields in the device, while we note that the experimental error due to strain is relatively large, and thus, determination of the direction of the strain field [5] is necessary to more precisely discuss the effect of N-ion implantation. In addition, superresolution techniques [45–47] will enable us to capture the electric field distribution in more detail, including the resonance difference for the N-V and V-N orientations and the high electric field at the concentrated region.

Finally, we estimate the electric field sensitivity. Considering the linear relationship between the ODMR frequency shift and the electric field as a simplified model, the shot noise limit sensitivity is described as [12,48]

$$\eta = \frac{4}{3\sqrt{3}} \frac{\Delta f}{k_\perp C \sqrt{R}}, \qquad (3)$$

where Δf and C are the line width and contrast of an ODMR signal, respectively. R is a photon count rate. While the ODMR shift is nonlinear against the electric field at around zero field, as observed in Fig. 4, the measurement in the linear relationship will be conducted by applying a bias field. Using the experimental result of N-V A at 0 V (Fig. 2), we obtain an electric field sensitivity of about $50 \, \text{kV/cm}/\sqrt{\text{Hz}}$ for a sensor area of approximately 1 μm^2. The dc sensitivity will be improved by various methods. The photon collection efficiency can be increased by using an oil objective lens to improve the photon count rate, although it cannot be applied for measurements in the vacuum chamber used in this study. Then, a pulsed ODMR technique significantly reduces the line width by avoiding MW-power broadening [49]. More dramatic improvement will be achieved by recently reported methods, i.e., Ramsey-based sensing in a dressed frame [18] or utilization of the electric field susceptibility in the excited state under resonant excitation [12]. The former method reduces noise from the magnetic field by a factor of about 700 [18]. In the latter method, the excited-state susceptibility is estimated to be approximately five orders of

magnitude larger than that in the ground state [12]. While they require a sophisticated pulse control or resonant excitation, measurements with a better electric field sensitivity are also expected to be applicable for vector electrometry. Nonetheless, one might benefit from continuous-wave ODMR for sensing a high electric field demonstrated in this study, since the signal shape of multiple dips from the target N-*V* centers can be directly observed.

V. CONCLUSIONS

We demonstrate vector electrometry in a vertical diamond *p-i-n* diode using an ensemble of N-*V* centers directly embedded in the device. Application of the transverse magnetic field to a target N-*V* axis enable us to identify the signals from the target in an ODMR spectrum and to enhance the ODMR response against the electric field, compared with the case for application of an axial magnetic field. By performing the process for multiple N-*V* axes, we successfully obtain the components of the electric field generated in the device and confirm that the experimental values are close to the simulation results of a structural model that includes the implanted N donors. The vector electrometry demonstrated here will become an important technique to reveal the electric fields generated in various systems.

ACKNOWLEDGMENTS

APPENDIX A: ODMR SPLIT WIDTH UNDER MAGNETIC AND ELECTRIC FIELDS

Under arbitrarily directed magnetic and electric fields, the ODMR splitting in an N-*V* coordinate is described as [7]

$$\frac{1}{2}W = \left[(\gamma^2 B_z^2 + k_\perp^2 \Pi_\perp^2) - \frac{\gamma^2 B_\perp^2}{2D_{GS}} (\gamma^2 B_z^2 + k_\perp^2 \Pi_\perp^2)^{\frac{1}{2}} \right.$$

$$\left. \times \sin\alpha \cos(2\phi_B + \phi_\Pi) + \frac{\gamma^4 B_\perp^4}{4D_{GS}^2} \right]^{\frac{1}{2}}, \quad \text{(A1)}$$

where B_z is the axial magnetic field along the N-*V* axis, $\tan\alpha = k_\perp \Pi_\perp / \gamma B_z$, and $\tan\phi_B = B_y / B_x$. Notably, an axial electric field leads to the center shift of the two

resonance frequencies [7], and thus, no effect is observed on splitting.

When taking $B_z \sim 0$, Eq. (A1) becomes

$$\frac{1}{2}W = \left[k_\perp^2 \Pi_\perp^2 - \frac{\gamma^2 B_\perp^2}{2D_{GS}} k_\perp \Pi_\perp \cos(2\phi_B + \phi_\Pi) + \frac{\gamma^4 B_\perp^4}{4D_{GS}^2} \right]^{\frac{1}{2}}. \quad \text{(A2)}$$

Setting the direction of the transverse magnetic field along the *x* axis in a target N-*V* alignment leads to $\cos(2\phi_B + \phi_\Pi) = \cos\phi_\Pi$. Consequently, we obtain Eq. (1) in the main text.

On the other hand, when an axial magnetic field is applied, the first and second terms on the right-hand side, $(\gamma^2 B_z^2 + k_\perp^2 \Pi_\perp^2)$, in Eq. (A1) become dominant, and Eq. (A1) is reduced to

$$\frac{1}{2}W \approx [\gamma^2 B_z^2 + k_\perp^2 \Pi_\perp^2]^{\frac{1}{2}}. \quad \text{(A3)}$$

This relation is illustrated as the dashed lines in Fig. 4. With a constant axial magnetic field, the increase in the split width is nonlinear against the effective electric field ($\Pi_\perp$) and becomes much lower than that for the case with a transverse magnetic field (solid lines).

APPENDIX B: MEASUREMENT SYSTEM

A schematic illustration of the measurement system in the vacuum chamber is shown in Fig. 6. The sample holder is designed to be equipped with three-axis electromagnets. A large coil placed at the center and four coils with iron cores control the magnetic field along the *z* axis and on the *x-y* plane in the lab frame, respectively. We determine the direction of the transverse magnetic field by observing the smallest splitting from the target N-*V* signals in
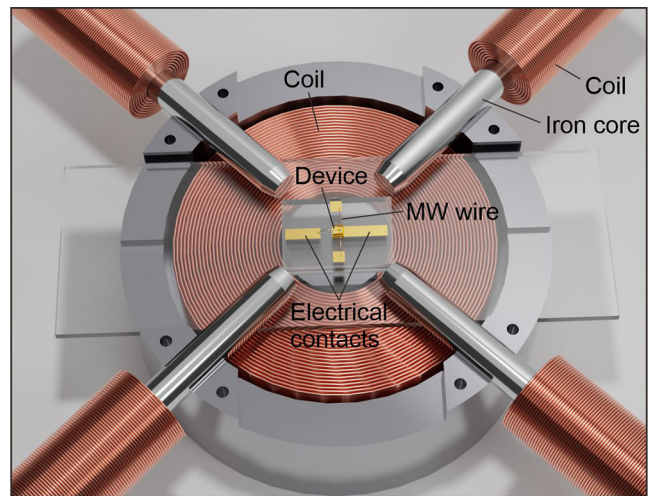

FIG. 6. Schematic of measurement system in the vacuum chamber.

the ODMR spectrum. The diamond devices have electrical contacts to apply a bias. MW radiation for the electron-spin resonance of the N-*V* centers is applied via a thin Cu wire. The microwave wire, electromagnets, and electrical contacts are connected to controllers outside the chamber through feedthrough connectors.

APPENDIX C: UNIT VECTORS

The unit vector for each N-*V* alignment in the lab frame defined in Fig. 1(d) is given as

$$\mathbf{u}_{\text{N-}VA} = \begin{pmatrix} 0 \\ 0 \\ -1 \end{pmatrix},$$

$$\mathbf{u}_{\text{N-}VB} = \begin{pmatrix} \sin\theta \\ 0 \\ -\cos\theta \end{pmatrix},$$

$$\mathbf{u}_{\text{N-}VC} = \begin{pmatrix} \sin\theta \cos 120° \\ \sin\theta \sin 120° \\ -\cos\theta \end{pmatrix},$$

$$\mathbf{u}_{\text{N-}VD} = \begin{pmatrix} \sin\theta \cos 240° \\ \sin\theta \sin 240° \\ -\cos\theta \end{pmatrix},$$

where $\theta = 109.47°$ corresponds to the angle between the N-*V* axes. By substituting into Eq. (2) and solving a system of equations, the components of the electric field (E_x, E_y, and E_z) can be calculated. E_y is negligible in the device used in this study. Thus, we estimate E_x and E_z using the two equations regarding N-*V A* and N-*V B*.

APPENDIX D: ELECTRICAL CHARACTERIZATION

Figure 7(a) shows an *I*-*V* curve of the vertical diamond *p*-*i*-*n* diode incorporating an ensemble of N-*V* centers. The current rapidly increases at a forward voltage of approximately −4 V, corresponding to the built-in potential of diamond. The device shows a high rectification ratio of about 10^6 at ±10 V, indicating good diode operation. The breakdown does not occur, even at a high voltage over 400 V [Fig. 7(b)]. The reverse current of devices at 100 V with different amounts of N-*V* centers is summarized in Fig. 7(c). Except for one clean device without the N-*V* center (no. 3), the reverse current is about 10^{-7} A. Thus, N-*V* fabrication does not affect the reverse current. Device no. 3 might possess defects in the device that cause the leakage path [50]. Notably, the difference in the current between Figs. 7(b) and 7(c) might be related to different measurement systems and diamond surface conditions.

APPENDIX E: SIMULATION MODEL

Figure 8 depicts the two structural models used for the device simulation. Model 1 is a normal *p*-*i*-*n* diode. The n^+ regions on top have a phosphorus concentration of 1×10^{19} cm^{-3}, and the *p* substrate is boron-doped, with a concentration of 1×10^{17} cm^{-3}. The boron concentration of the *i* layer is 2×10^{14} cm^{-3}, which is the detection limit of secondary-ion mass spectrometry. In model 2, the nitrogen donors are included in the *i* layer and at the n^+-*i* interface, with a projected depth of 350 nm. These two models define the boundaries of the electric field
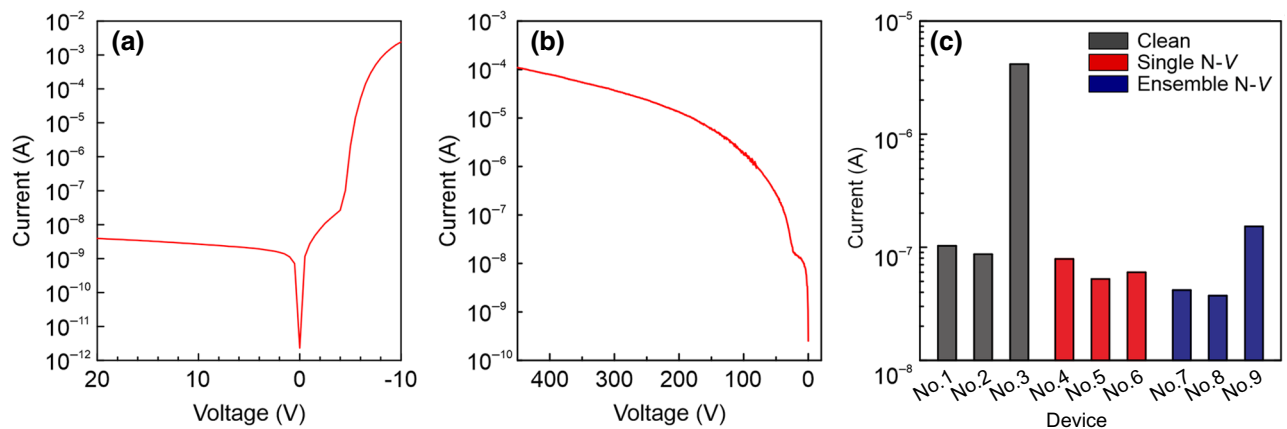

FIG. 7. Electrical characteristics of diamond *p*-*i*-*n* diodes. (a) *I*-*V* curve of a device with ensemble N-*V* centers, measured using a vacuum probe system. (b) High-voltage property of a device with ensemble N-*V* centers, measured in the vacuum chamber for electric field sensing. (c) Current at a reverse bias of 100 V of devices with different N-*V* amounts, measured in a vacuum probe system. Clean, Single N-*V*, and Ensemble N-*V* denote the device without N-ion implantation, with a N dose of 1×10^9 cm^{-2} and with a N dose of 1×10^{12} cm^{-2}, respectively.
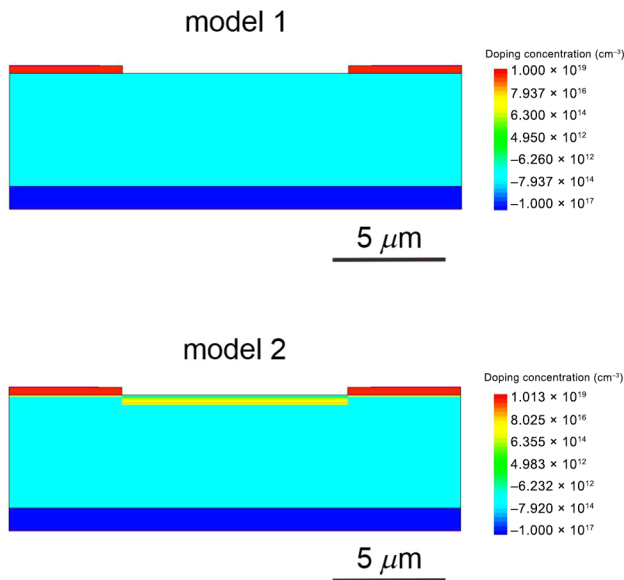
model 1

model 2

FIG. 8. Structural models in the simulation, showing the doping concentrations. The positive and negative values correspond to the donor and acceptor concentrations, respectively.

simulation, and the values with intermediate nitrogen concentrations are between the two models. We find that, in model 2, E_x takes negative values at low voltages, depending on the nitrogen concentration and, then, it becomes positive as the voltage increases. This finding explains why the E_x values in model 2 are lower than those in model 1 in Fig. 5(b). As expected, however, application of a voltage of 400 V leads to a positive E_x value.

APPENDIX F: SPATIAL RESOLUTION

Figure 9(a) shows a CCD image of an array of N-V centers in a diamond transistor fabricated on a Ib-type diamond substrate [51] formed by the gas-field ion-source-focused ion beam (GFIS FIB) technique [52]. The focused nitrogen ions are implanted with 800 nm pitch, which is confirmed by confocal fluorescence microscopy observations. Figure 9(b) shows an intensity profile along a dashed line in Fig. 9(a). The four N-V fluorescence peaks are observed, corresponding to the bright spots in Fig. 9(a). The full width at half maximum of a spot is approximately 420 nm, which is close to the diffraction limit ($\sim$350 nm). However, we note that a slight drift occurs along the z direction in the lab frame during the electric field measurements, especially when we apply a magnetic field along the z direction using a large coil. Thus, the spatial resolution of the electric field measurements is expected to be of micrometer scale.
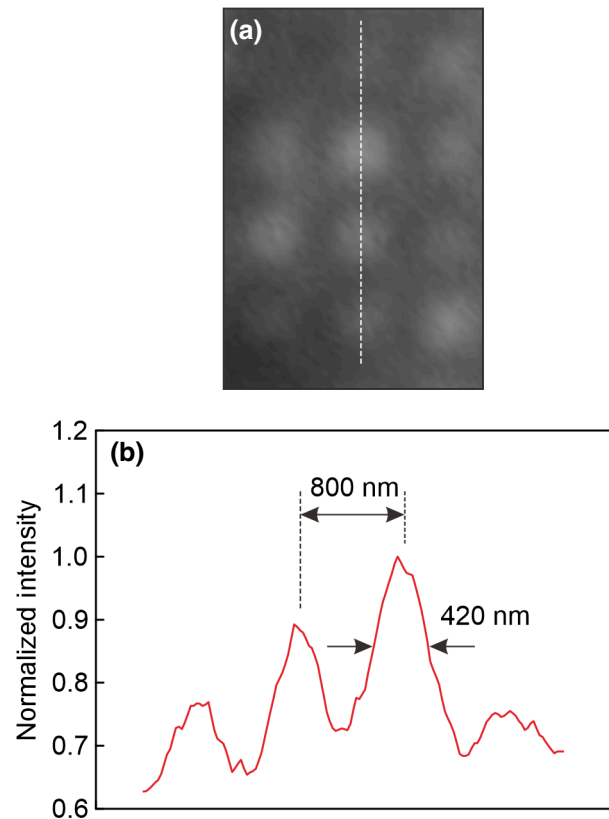

FIG. 9. N-V array formed by GFIS FIB. (a) CCD image. (b) Intensity profile along the dashed line in (a).

[1] J. A. Slinkman, C. C. Williams, D. W. Abraham, and H. K. Wickramasinghe, Lateral dopant profiling in MOS structures on a 100 nm scale using scanning capacitance microscopy, Tech. Dig. - Int. Electron Devices Meet. 73 (1990).

[2] A. K. Henning, T. Hochwitz, J. Slinkman, J. Never, S. Hoffmann, P. Kaszuba, and C. Daghlian, Two-Dimensional surface dopant profiling in silicon using scanning kelvin probe microscopy, J. Appl. Phys. **77**, 1888 (1995).

[3] R. P. Dwyer, L. M. Smieska, A. M. Tirmzi, and J. A. Marohn, Vector electric field measurement via position-modulated kelvin probe force microscopy, Appl. Phys. Lett. **111**, 173106 (2017).

[4] E. Van Oort and M. Glasbeek, Electric-Field-Induced modulation of spin echoes of N-V centers in diamond, Chem. Phys. Lett. **168**, 529 (1990).

[5] F. Dolde, H. Fedder, M. W. Doherty, T. Nöbauer, F. Rempp, G. Balasubramanian, T. Wolf, F. Reinhard, L. C. L. Hollenberg, F. Jelezko, and J. Wrachtrup, Electric-Field sensing using single diamond spins, Nat. Phys. **7**, 459 (2011).

[6] F. Dolde, M. W. Doherty, J. Michl, I. Jakobi, B. Naydenov, S. Pezzagna, J. Meijer, P. Neumann, F. Jelezko, N. B. Manson, and J. Wrachtrup, Nanoscale Detection of a Single Fundamental Charge in Ambient Conditions Using the NV - Center in Diamond, Phys. Rev. Lett. **112**, 097603 (2014).

[7] M. W. Doherty, J. Michl, F. Dolde, I. Jakobi, P. Neumann, N. B. Manson, and J. Wrachtrup, Measuring the defect structure orientation of a single NV- centre in diamond, New J. Phys. **16**, 063067 (2014).

[8] E. H. Chen, H. A. Clevenson, K. A. Johnson, L. M. Pham, D. R. Englund, P. R. Hemmer, and D. A. Braje, High-Sensitivity spin-based electrometry with an ensemble of nitrogen-vacancy centers in diamond, Phys. Rev. A **95**, 053417 (2017).

[9] T. Iwasaki, W. Naruki, K. Tahara, T. Makino, H. Kato, M. Ogura, D. Takeuchi, S. Yamasaki, and M. Hatano, Direct nanoscale sensing of the internal electric field in operating semiconductor devices using single electron spins, ACS Nano **11**, 1238 (2017).

[10] D. A. Broadway, N. Dontschuk, A. Tsai, S. E. Lillie, C. T. K. Lew, J. C. McCallum, B. C. Johnson, M. W. Doherty, A. Stacey, L. C. L. Hollenberg, and J. P. Tetienne, Spatial mapping of band bending in semiconductor devices using in situ quantum sensors, Nat. Electron. **1**, 502 (2018).

[11] J. Michl, J. Steiner, A. Denisenko, A. Bülau, A. Zimmermann, K. Nakamura, H. Sumiya, S. Onoda, P. Neumann, J. Isoya, and J. Wrachtrup, Robust and accurate electric field sensing with solid state spin ensembles, Nano Lett. **19**, 4904 (2019).

[12] M. Block, B. Kobrin, A. Jarmola, S. Hsieh, C. Zu, N. L. Figueroa, V. M. Acosta, J. Minguzzi, J. R. Maze, D. Budker, and N. Y. Yao, Optically enhanced electric field sensing using nitrogen-vacancy ensembles, ArXiv:2004.02886 (2020).

[13] P. Jamonneau, M. Lesik, J. P. Tetienne, I. Alvizu, L. Mayer, A. Dréau, S. Kosen, J. F. Roch, S. Pezzagna, J. Meijer, T. Teraji, Y. Kubo, P. Bertet, J. R. Maze, and V. Jacques, Competition between electric field and magnetic field noise in the decoherence of a single spin in diamond, Phys. Rev. B **93**, 024305 (2016).

[14] T. Mittiga, S. Hsieh, C. Zu, B. Kobrin, F. Machado, P. Bhattacharyya, N. Z. Rui, A. Jarmola, S. Choi, D. Budker, and N. Y. Yao, Imaging the Local Charge Environment of Nitrogen-Vacancy Centers in Diamond, Phys. Rev. Lett. **121**, 246402 (2018).

[15] M. Kim, H. J. Mamin, M. H. Sherwood, K. Ohno, D. D. Awschalom, and D. Rugar, Decoherence of Near-Surface Nitrogen-Vacancy Centers Due to Electric Field Noise, Phys. Rev. Lett. **115**, 087602 (2015).

[16] J. Forneris, S. Ditalia Tchernij, P. Traina, E. Moreva, N. Skukan, M. Jakšić, V. Grilj, F. Bosia, E. Enrico, G. Amato, I. P. Degiovanni, B. Naydenov, F. Jelezko, M. Genovese, and P. Olivero, Mapping the Local Spatial Charge in Defective Diamond by Means of N- v Sensors - A Self-Diagnostic Concept, Phys. Rev. Appl. **10**, 014024 (2018).

[17] L. M. Oberg, M. O. De Vries, L. Hanlon, K. Strazdins, M. S. J. Barson, M. W. Doherty, and J. Wrachtrup, Solution to Electric Field Screening in Diamond Quantum Electrometers, Phys. Rev. Appl. **14**, 1 (2020).

[18] R. Li, F. Kong, P. Zhao, Z. Cheng, Z. Qin, M. Wang, Q. Zhang, P. Wang, Y. Wang, F. Shi, and J. Du, Nanoscale Electrometry Based on a Magnetic-Field-Resistant Spin Sensor, Phys. Rev. Lett. **124**, 247701 (2020).

[19] G. Wolfowicz, S. J. Whiteley, and D. D. Awschalom, Electrometry by optical charge conversion of deep defects in 4H-SiC, Proc. Natl. Acad. Sci. U. S. A. **115**, 7879 (2018).

[20] G. Wolfowicz, C. P. Anderson, S. J. Whiteley, and D. D. Awschalom, Heterodyne detection of radio-frequency electric fields using point defects in silicon carbide, Appl. Phys. Lett. **115**, 043105 (2019).

[21] M. W. Doherty, F. Dolde, H. Fedder, F. Jelezko, J. Wrachtrup, N. B. Manson, and L. C. L. Hollenberg, Theory of the ground-state spin of the NV - center in diamond, Phys. Rev. B **85**, 205203 (2012).

[22] J. R. Maze, P. L. Stanwix, J. S. Hodges, S. Hong, J. M. Taylor, P. Cappellaro, L. Jiang, M. V. G. Dutt, E. Togan, A. S. Zibrov, A. Yacoby, R. L. Walsworth, and M. D. Lukin, Nanoscale magnetic sensing with an individual electronic spin in diamond, Nature **455**, 644 (2008).

[23] G. Balasubramanian, I. Y. Chan, R. Kolesov, M. Al-Hmoud, J. Tisler, C. Shin, C. Kim, A. Wojcik, P. R. Hemmer, A. Krueger, T. Hanke, A. Leitenstorfer, R. Bratschitsch, F. Jelezko, and J. Wrachtrup, Nanoscale imaging magnetometry with diamond spins under ambient conditions, Nature **455**, 648 (2008).

[24] J. M. Taylor, P. Cappellaro, L. Childress, L. Jiang, D. Budker, P. R. Hemmer, A. Yacoby, R. Walsworth, and M. D. Lukin, High-Sensitivity diamond magnetometer with nanoscale resolution, Nat. Phys. **4**, 810 (2008).

[25] G. Kucsko, P. C. Maurer, N. Y. Yao, M. Kubo, H. J. Noh, P. K. Lo, H. Park, and M. D. Lukin, Nanometre-Scale thermometry in a living cell, Nature **500**, 54 (2013).

[26] M. W. Doherty, V. M. Acosta, A. Jarmola, M. S. J. Barson, N. B. Manson, D. Budker, and L. C. L. Hollenberg, Temperature shifts of the resonances of the NV-center in diamond, Phys. Rev. B **90**, 041201(R) (2014).

[27] A. Brunner, J. H. Shim, D. Suter, H. Sumiya, J. Isoya, and J. Wrachtrup, High-Precision nanoscale temperature sensing using single defects in diamond, Nano Lett. **13**, 2738 (2013).

[28] V. M. Acosta, E. Bauch, M. P. Ledbetter, A. Waxman, L. S. Bouchard, and D. Budker, Temperature Dependence of the Nitrogen-Vacancy Magnetic Resonance in Diamond, Phys. Rev. Lett. **104**, 070801 (2010).

[29] D. M. Toyli, D. J. Christle, A. Alkauskas, B. B. Buckley, C. G. Van de Walle, and D. D. Awschalom, Measurement and control of single nitrogen-vacancy center spins above 600 K, Phys. Rev. X **2**, 031001 (2012).

[30] M. W. Doherty, V. V. Struzhkin, D. A. Simpson, L. P. McGuinness, Y. Meng, A. Stacey, T. J. Karle, R. J. Hemley, N. B. Manson, L. C. L. Hollenberg, and S. Prawer, Electronic Properties and Metrology Applications of the Diamond NV - Center Under Pressure, Phys. Rev. Lett. **112**, 047601 (2014).

[31] M. Willander, M. Friesel, Q. U. Wahab, and B. Straumal, Silicon carbide and diamond for high temperature device applications, J. Mater. Sci. Mater. Electron. **17**, 1 (2006).

[32] A. Hiraiwa and H. Kawarada, Blocking characteristics of diamond junctions with a punch-through design, J. Appl. Phys. **117**, 124503 (2015).

[33] B. Grotz, M. V. Hauf, M. Dankerl, B. Naydenov, S. Pezzagna, J. Meijer, F. Jelezko, J. Wrachtrup, M. Stutzmann, F. Reinhard, and J. A. Garrido, Charge state manipulation of qubits in diamond, Nat. Commun. **3**, 729 (2012).

[34] C. Schreyvogel, M. Wolfer, H. Kato, M. Schreck, and C. E. Nebel, Tuned NV emission by In-plane Al-schottky

junctions on hydrogen terminated diamond, Sci. Rep. **4**, 3634 (2014).

[35] N. Mizuochi, T. Makino, H. Kato, D. Takeuchi, M. Ogura, H. Okushi, M. Nothaft, P. Neumann, A. Gali, F. Jelezko, J. Wrachtrup, and S. Yamasaki, Electrically driven single-photon source at room temperature in diamond, Nat. Photonics **6**, 299 (2012).

[36] H. Kato, M. Wolfer, C. Schreyvogel, M. Kunzer, W. Müller-Sebert, H. Obloh, S. Yamasaki, and C. Nebel, Tunable light emission from nitrogen-vacancy centers in single crystal diamond PIN diodes, Appl. Phys. Lett. **102**, 151101 (2013).

[37] E. Bourgeois, A. Jarmola, P. Siyushev, M. Gulka, J. Hruby, F. Jelezko, D. Budker, and M. Nesladek, Photoelectric detection of electron spin resonance of nitrogen-vacancy centres in diamond, Nat. Commun. **6**, 8577 (2015).

[38] F. M. Hrubesch, G. Braunbeck, M. Stutzmann, F. Reinhard, and M. S. Brandt, Efficient Electrical Spin Readout of NV-Centers in Diamond, Phys. Rev. Lett. **118**, 037601 (2017).

[39] P. Siyushev, M. Nesladek, E. Bourgeois, M. Gulka, J. Hruby, T. Yamamoto, M. Trupke, T. Teraji, J. Isoya, and F. Jelezko, Photoelectrical imaging and coherent spin-state readout of single nitrogen-vacancy centers in diamond, Science **363**, 728 (2019).

[40] H. Morishita, S. Kobayashi, M. Fujiwara, H. Kato, T. Makino, S. Yamasaki, and N. Mizuochi, Room temperature electrically detected nuclear spin coherence of NV centres in diamond, Sci. Rep. **10**, 792 (2020).

[41] B. J. Maertz, A. P. Wijnheijmer, G. D. Fuchs, M. E. Nowakowski, and D. D. Awschalom, Vector magnetic field microscopy using nitrogen vacancy centers in diamond, Appl. Phys. Lett. **96**, 092504 (2010).

[42] J. M. Schloss, J. F. Barry, M. J. Turner, and R. L. Walsworth, Simultaneous Broadband Vector Magnetometry Using Solid-State Spins, Phys. Rev. Appl. **10**, 034044 (2018).

[43] J. Michl, T. Teraji, S. Zaiser, I. Jakobi, G. Waldherr, F. Dolde, P. Neumann, M. W. Doherty, N. B. Manson, J. Isoya, and J. Wrachtrup, Perfect alignment and preferential orientation of nitrogen-vacancy centers during chemical vapor deposition diamond growth on (111) surfaces, Appl. Phys. Lett. **104**, 102407 (2014).

[44] M. Shimizu, T. Makino, T. Iwasaki, J. Hasegawa, K. Tahara, W. Naruki, H. Kato, S. Yamsaki, and M. Hatano, Diamond & related materials charge state modulation of nitrogen vacancy centers in diamond by applying a forward voltage across a $p-i-n$ junction, Diam. Relat. Mater. **63**, 192 (2016).

[45] S. Arroyo-Camejo, M. P. Adam, M. Besbes, J. P. Hugonin, V. Jacques, J. J. Greffet, J. F. Roch, S. W. Hell, and F. Treussart, Stimulated emission depletion microscopy resolves individual nitrogen vacancy centers in diamond nanocrystals, ACS Nano **7**, 10912 (2013).

[46] M. Pfender, N. Aslam, G. Waldherr, P. Neumann, and J. Wrachtrup, Single-Spin stochastic optical reconstruction microscopy, Proc. Natl. Acad. Sci. U. S. A. **111**, 14669 (2014).

[47] K. Arai, C. Belthangady, H. Zhang, N. Bar-Gill, S. J. DeVience, P. Cappellaro, A. Yacoby, and R. L. Walsworth, Fourier magnetic imaging with nanoscale resolution and compressed sensing speed-up using electronic spins in diamond, Nat. Nanotechnol. **10**, 859 (2015).

[48] J. F. Barry, J. M. Schloss, E. Bauch, M. J. Turner, C. A. Hart, L. M. Pham, and R. L. Walsworth, Sensitivity optimization for NV-diamond magnetometry, Rev. Mod. Phys. **92**, 15004 (2020).

[49] A. Dréau, M. Lesik, L. Rondin, P. Spinicelli, O. Arcizet, J. F. Roch, and V. Jacques, Avoiding power broadening in optically detected magnetic resonance of single NV defects for enhanced dc magnetic field sensitivity, Phys. Rev. B **84**, 195204 (2011).

[50] T. Iwasaki, T. Suwa, J. Yaita, H. Kato, T. Makino, M. Ogura, D. Takeuchi, S. Yamasaki, and M. Hatano, Observation of interface defects in diamond lateral P-n-junction diodes and their effect on reverse leakage current, IEEE Trans. Electron Devices **64**, 3298 (2017).

[51] T. Iwasaki, J. Yaita, H. Kato, T. Makino, M. Ogura, D. Takeuchi, H. Okushi, S. Yamasaki, and M. Hatano, 600 V diamond junction field-effect transistors operated at 200 °C, IEEE Electron Device Lett. **35**, 241 (2014).

[52] M. E. Schmidt, M. Akabori, and H. Mizuta, in *Ion Beam Applications*, edited by I. Ahmad, M. Maaza (Intech, London, 2018), pp. 113–135.